geosciences

Article

Multitemporal Quantification of the Geomorphodynamics on a Slope within the Cratère Dolomieu at the Piton de la Fournaise (La Réunion, Indian Ocean) Using Terrestrial LiDAR Data, Terrestrial Photographs, and Webcam Data

Kerstin Wegner [1,*], Virginie Durand [2,3], Nicolas Villeneuve [3,4,5], Anne Mangeney [3], Philippe Kowalski [3,5], Aline Peltier [3,5], Manuel Stark [1], Michael Becht [1] and Florian Haas [1]

[1] Physical Geography, Catholic University of Eichstaett Ingolstadt, 85072 Eichstaett, Germany
[2] Geo Seismic—Cycles, Université Côte d'Azur, IRD, CNRS, Observatoire de la Côte d'Azur, Géoazur, 06560 Sophia-Antipolis, France
[3] Institut de Physique du Globe de Paris, Université Paris Cité, CNRS, 75005 Paris, France; nicolas.villeneuve@univ-reunion.fr (N.V.); anne.mangeney@gmail.com (A.M.)
[4] Laboratoire GéoSciences Réunion, Université de La Réunion, 97744 Saint Denis, France
[5] Observatoire Volcanologique du Piton de la Fournaise, Institut de Physique du Globe de Paris, 97418 La Plaine des Cafres, France
* Correspondence: kwegner@ku.de

Abstract: In this study, the geomorphological evolution of an inner flank of the Cratère Dolomieu at Piton de La Fournaise/La Réunion was investigated with the help of terrestrial laser scanning (TLS) data, terrestrial photogrammetric images, and historical webcam photographs. While TLS data and the terrestrial images were recorded during three field surveys, the study was also able to use historical webcam images that were installed for the monitoring of the volcanic activity inside the crater. Although the webcams were originally intended to be used only for visual monitoring of the area, at certain times they captured image pairs that could be analyzed using structure from motion (SfM) and subsequently processed to create digital terrain models (DTMs). With the help of all the data, the geomorphological evolution of selected areas of the crater was investigated in high temporal and spatial resolution. Surface changes were detected and quantified on scree slopes in the upper area of the crater as well as on scree slopes at the transition from the slope to the crater floor. In addition to their quantification, these changes could be assigned to individual geomorphological processes over time. The webcam photographs were a very important additional source of information here, as they allowed the observation period to be extended further into the past. Besides this, the webcam images made it possible to determine the exact dates at which geomorphological processes were active.

Keywords: terrestrial images; webcam data; LiDAR; TLS; photogrammetry; structure from motion; rockfalls; multitemporal change detection

check for updates

Citation: Wegner, K.; Durand, V.; Villeneuve, N.; Mangeney, A.; Kowalski, P.; Peltier, A.; Stark, M.; Becht, M.; Haas, F. Multitemporal Quantification of the Geomorphodynamics on a Slope within the Cratère Dolomieu at the Piton de la Fournaise (La Réunion, Indian Ocean) Using Terrestrial LiDAR Data, Terrestrial Photographs, and Webcam Data. *Geosciences* **2024**, *14*, 259. https://doi.org/10.3390/geosciences14100259

Received: 8 August 2024
Revised: 11 September 2024
Accepted: 24 September 2024
Published: 28 September 2024

1. Introduction

Slopes in high mountain and volcanic regions are formed by a variety of geomorphological processes and their interaction. Forming and evolving craters and calderas are important geomorphic processes in volcanic regions. Gravitational instabilities can be induced by ongoing deformation and other processes affecting volcanic surfaces [1–3]. Observations have shown that calderas form mainly by subsidence, caused by magma draining from an underlying reservoir causing the overlying rock to collapse [4–7]. This collapse creates steep slopes susceptible to continuous rockfall and debris flows, for example, leading to deposits within the caldera [7]. In general, two main types of processes, depending on their occurrence and amplitude, govern the construction and evolution of high mountain slopes. There are high-frequency, low-amplitude phenomena that are constantly monitored, measured, and quantified [8]. However, there are also low-frequency, high-amplitude events that are measured only sporadically [9–12]. For example, fluvial erosion contrasts with landslides and other debris avalanches. Infrequent processes such as debris flows or rockfalls can affect a high proportion of the sediment balance. Both the magnitude and frequency of these events are of great scientific interest, and this is why they are quantified in numerous studies, whereby different approaches are used [13].

It is possible to identify and map individual events of high magnitude using archival data such as historical aerial photographs, historical airborne laser scanning (ALS) data, photographs, or written records, e.g., [3,14–18]. Quantities of transported material can be derived from diachronic digital terrain models (DTMs) obtained by LiDAR (light detection and raging) acquisitions and/or stereophotogrammetric (SfM: structure from motion) analyses. However, the exact localization of the event can be used to determine the transported quantities at least approximately with current 3D surveys, e.g., [16]. In addition, it is necessary to consider the importance of the timing of the event's occurrence. It is essential that this is defined as accurately as possible. Due to this difficulty, it is important to note that temporal precision hinges on the temporal resolution of the input data. Depending on the region, time series of high-resolution aerial photographs can be available with an interval of several decades [13,16], whereas newer ALS data have intervals of up to a decade. This makes it difficult to determine the recurrence probability of such larger events accurately.

In addition to the fact that the frequency is not precisely recordable, there is a further problem in high mountain regions due to the usually very high geomorphodynamics. On steep and vegetation-free slopes, such as those of the Cratère Dolomieu of Piton de la Fournaise (PLF), individual processes may occur in succession, making it difficult to differentiate them. This problem is even more significant when the frequency of event occurrence is much higher than that of data acquisition. Consequently, this leads to inaccuracies regarding the frequency and magnitude of recorded events and, accordingly, in the data processing [19]. The probability of multiple events occurring between two measurement campaigns (especially several small ones that are not identified at the time of their occurrence and are later obscured by a larger one) is very high. This directly increases the error in calculating the frequency of occurrence [19].

Seismometers are therefore increasingly being used to monitor the frequency and magnitude of gravitational mass movements, e.g., [20–23]. These measurements make it possible to localize such events (starting zone, process area) precisely and to quantify them accurately using the seismic signals [24]. In addition to seismometers, InSAR (Interferometric Synthetic Aperture Radar) data can be used to monitor calderas [25,26].

Terrestrial photographs are another possibility to record changes on steep slopes, e.g., [16,18,27,28], but often have low temporal resolution, even for well-known locations like, e.g., famous alpine peaks [18]. While these images can extend observation series into the past, they cannot provide high temporal densification. In contrast, webcams (automatic cameras) used over the past 30 years offer a solution [29–32]. The prerequisites for the use of such data are (i) the longest possible period of time over which a webcam was operated at a fixed location and (ii) that the data were appropriately saved over this period. If these conditions are fulfilled, single images can be used for detailed spatial mapping and identification of single events, e.g., by visual inspection with a very high temporal resolution. This allows precise determination of event frequency in time and magnitude through subsequent quantification via, e.g., SfM or LiDAR. If such webcam images are available in pairs, direct quantitative analyses can be performed on the overlapping areas using a more or less 4D approach. In most cases, such image pairs are not installed according to stereophotogrammetric principles. Instead, they are captured to represent a slope from different angles or to view larger slope sections, which can result in overlaps that can in turn be used (with restrictions) for stereophotogrammetric processing.

Although there are some studies that use fixed webcams for volcano monitoring, these are not for the purpose of multitemporal analysis and quantification of geomorphological processes [33–36]. For this reason, this study used two webcams in combination with additional data such as terrestrial LiDAR and terrestrial photography within the Cratère Dolomieu at PLF. The aim was to determine the geomorphodynamics of a slope over a period of approximately six years (2010–2016). In addition, the study aimed to investigate whether these photographs can help to analyze geomorphodynamics at a higher temporal resolution.

2. Study Area

La Réunion is a tropical island located in the Indian Ocean east of Madagascar (Figure 1). It forms an oceanic shield volcano with a spatial extent of nearly 240 km in diameter and a height of seven km measured from the seafloor [37,38]. The island has an age of around five Ma [39], beginning with the growth of the adjacent volcanoes Piton des Neiges (PDN) and Les Alizés (LA). While LA is now completely dismantled [37], PDN has remained inactive since its last eruption 27 ka years ago [40] but still forms the highest peak of La Réunion with about 3070 m a.s.l. All eruptions during the last 27 ka took place at PLF, which is situated on the flanks of LA and PDN and has a height of 2632 m a.s.l. PLF is among the most active shield volcanoes of the world [41] with a high eruptive frequency of one eruption every eight months on average [21]. The Cratère Dolomieu of PLF in its present shape (Figure 1) was partly formed by a collapse during an eruption in April 2007 and has partially begun to fill up due to lava flows of following eruptions [42]. The collapse of the crater floor created steep rock faces up to 320 m high, which are prone to continuous rockfall activity, varying widely in volume [22].

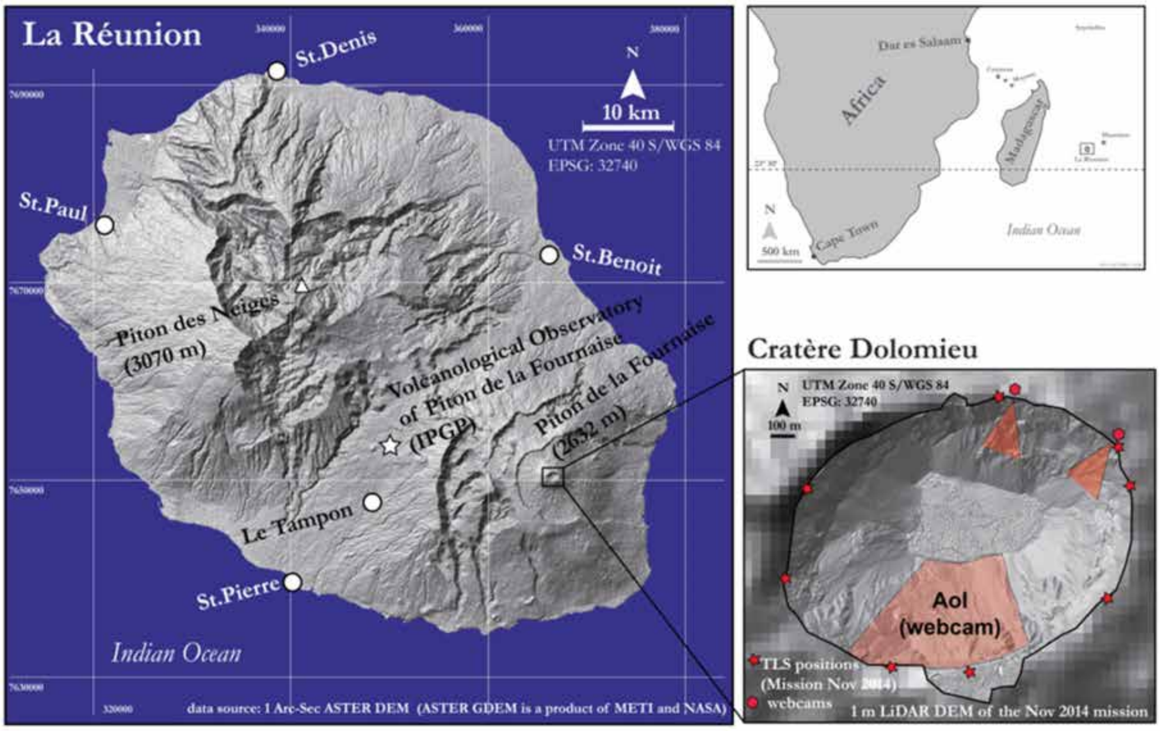

Figure 1. Location of the study area Cratère Dolomieu of the PLF. (Source of the overview base map: ASTER DEM. Source of the overview map of the Cratère Dolomieu is a 1 m DEM based on terrestrial laser scanning data acquired in 2014).

In addition to the volcanic filling of the caldera, geomorphic processes are involved in reshaping the "fresh" landscape inside the crater, characterized by high magnitudes and short frequencies. The very high geomorphic activity, resulting in massive slope failures and corresponding talus cones, is due to seismicity combined with the lithological and topographical conditions, as well as the extremely high amounts of rainfall [21,22]. The average annual precipitation ranges between 3000 and 4250 mm/year (for a watershed of the PLF catchment area, [43]) with particularly intense precipitation during the rainy season. Reference [44] measured a mean annual rainfall of 6200 mm. The climate station on the southern rim of the Cratère Dolomieu (Figure 1) recorded an annual mean precipitation of 7469 mm for the period 2010 until 2016 with a maximum of 9890 mm in 2015.

3. Materials and Methods

3.1. Acquisition and Registration of Ground-Based LiDAR Data

During a two-day mission in November 2014, the Cratère Dolomieu was captured by the terrestrial laser scanner (TLS) Riegl VZ4000 with a maximum scanning distance up to 4000 m. Stable, precipitation-free weather conditions had to prevail during the entire data acquisition period. The position of the sun also had to be taken into account in order to avoid excessive shading. Both the TLS data and the terrestrial photographs were taken by climbing up to the crater.

To provide a high-resolution point cloud of the whole crater and to minimize shadowing effects (c.f. [45]), the scanning was conducted from eight different scan positions, which were all located close to the crater rim (Figures 1 and 2). The TLS specifications and survey parameters are listed in Tables 1 and 2. The horizontal and vertical scan resolution was set to a 0.02° step width and included overlapping areas between the single scans and also areas in the backside of every scan position. The backside scans were captured in order to scan tie points (Riegl reflectors). Those exact positions of the reflectors were measured externally during the mission by using a dGNSS system (Figure 2) and thus provide information about the global coordinate system (UTM40S/WGS84; EPSG: 32740) after postprocessing. The acquired TLS raw data had to pass several postprocessing steps (c.f. [45]), beginning with the registration/referencing of every single scan position by using an iterative closest point (ICP) algorithm (Multi Station Adjustment tool) in the software RiScan Pro (Version 2.4, riegl.com) [46,47]. The referencing accuracies show values between 0.007 m and 0.013 m.

Figure 2. Riegl VZ4000 laser scanner located on the crater rim and dGNSS measurement of tie points (Riegl reflector) (own photographs captured during fieldwork in 2014).

After the registration and the merging of all scan positions, the resulting raw point cloud was linked with global coordinates by using dGNSS measured reflectors of four backside scans. After the processing procedure, the data were ASCII formatted (x, y, z, RGB values) and exported as global coordinates. The LiDAR point clouds had to be rotated in order to receive a z coordinate that is perpendicular to the rock face [49]. Ground control points (GCPs) were extracted from the LiDAR point cloud for georeferencing and scaling of the rock faces. These selected GCPs were also used for further SfM processing. All further processing steps (e.g., thinning, filtering, DEM generation) were performed using LIS Desktop/SAGA GIS (c.f. 3.5).

Table 1. Specifications of the TLS Riegl VZ-4000 [48]. The values given are based on measurements taken at a rate of 30 kHz (* = milliradian).

Parameter	Riegl VZ-4000
Max. measurement range	4000 m
Min. measurement range	5 m
Field of view	60° (vertical) × 360° (horizontal)
Measurement rate	Max. 230,000 pts./s
Accuracy	15 mm
Precision	10 mm
Laser wavelength	Near-infrared
Laser beam divergence	0.15 mrad *

Table 2. Survey parameters of TLS.

Survey Parameter	
No. of scan positions	8
No. of backside scans	8
Humidity	30%
Temperature	28 °C
Year	2014

3.2. Acquisition of Terrestrial Photographs

During missions in 2014 (at the same time as the TLS mission), 2015, and 2016 (additional missions without TLS acquisition) terrestrial photographs were captured around the crater rim, including all scan positions but also locations between them. Three different uncalibrated cameras were used for these images (Table 3). For this work, only pictures of the east-facing slope (2014 and 2016) as well as of the north-facing slope (same section as the webcams, 2010–2016, c.f. 3.3) were used for the following processing steps, which all pictures had to pass in order to produce SfM-based point clouds (c.f. 3.4).

Table 3. Three different camera systems used to capture the terrestrial photographs.

Parameters	Webcam	Webcam	Camera System 3	Camera System 4	Camera System 5
Type	Pentax	Canon	Pentax	Canon	Nikon
Name	K200D	EOS350D	Kx	EOS 1DS Mark III	D610
Resolution	10.2 MP	8 MP	12.2 MP	21.1 MP	24.3 MP
Focal length	18 mm	20 mm	28 mm	35 mm	32 mm
Exposure	1/200	1/40	1/200	1/100	1/400
Responsivity	100	100	200	100	100
Aperture	F/8	F/16	F/11	F/8	F/4.5
Amount of pictures	390	485	496	92	133
Amount of pictures used for data processing	2 pairs	4 pairs	4 pieces	4 pieces	4 pieces
Year	10/2009–07/2010	12/2010–12/2011	2014	2015	2016

3.3. Acquisition of Webcam Photographs

Between 2009 and 2012, a large number of photographs (875) were captured by two webcams located at the northern rim of the Cratère Dolomieu, focusing on the northern exposed slopes (Figure 1). During this period, different types of non-calibrated SLR cameras were used (Table 3). Parameters of the webcam-based camera systems are given in Table 3. Both camera setups were configured as time-lapse cameras with a fixed interval but without synchronization. Since the cameras were not originally intended for photogrammetric imaging, but rather to observe different zones of the southwestern crater, they did not operate in parallel for the entire period. This was compounded by data outages. On most days of both years, two pictures were available from each camera. However, due to the rapidly changing weather conditions on PLF, shadowing effects, and the lack of synchronization (resulting in different lightning conditions), only a few photographs were suitable for processing with SfM (4D analysis) (Table 3). Even though only a few photos could be used for the 4D analysis, individual photos still proved to be very helpful. They allowed for better visual classification of events over time, even if only partially.

3.4. SfM and Global Registration of the Point Clouds

To produce 3D point clouds from both the terrestrial and the webcam photographs, the following processing steps were performed using Agisoft Metashape Professional (AMP; Agisoft/Vers. 1.2.3-64bit). The overall data processing workflow for this study is shown in Figure 3.

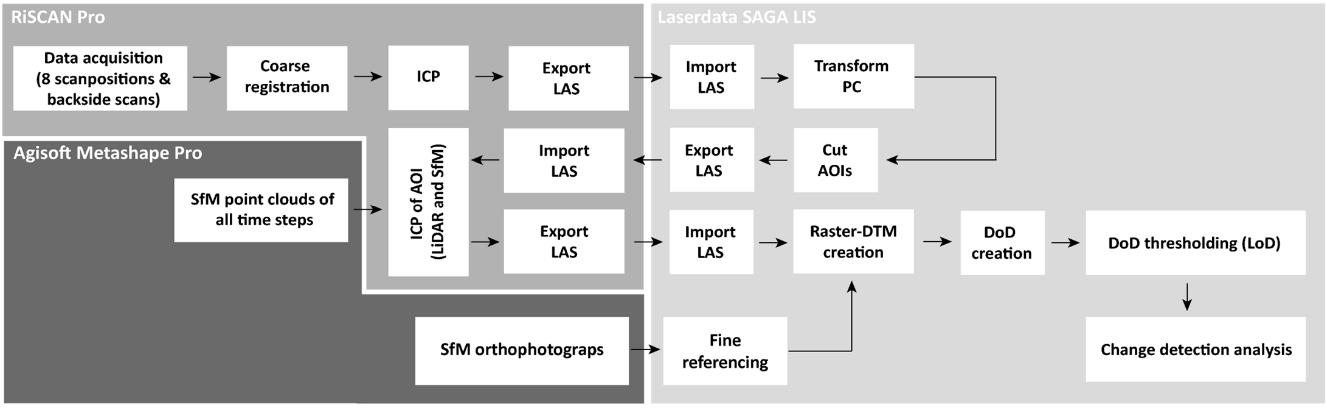

Figure 3. The entire workflow for processing TLS data, digital terrestrial, and webcam photographs is illustrated. The particular processing steps are demonstrated for each relevant software (RiSCAN PRO (Version 2.4), Agisoft Metashape Pro (Version 1.5.5), Laserdata SAGA LIS (Version 3.0.7, 3.1.0)).

- Pictures from each time step were aligned, and tie points were automatically derived by AMP, resulting in a first sparse point cloud, but still without a global referencing.
- GCPs were set on every single picture. Since it is not allowed to enter the crater, there are no markers available inside it. Thus, GCPs were first selected using concise objects in the 2014 TLS point cloud. The GCPs derived from the TLS point cloud were employed for scene triangulation and reconstruction [50], as well as for defining and adjusting the external orientation parameters (scale, rotation, translation) of the image sets [51]. The coordinates of the GCPs were obtained for structures that were clearly visible in both the TLS point cloud and the terrestrial photographs and had remained unchanged throughout the observation period. The criterion for the selection was the visibility of the concise objects/formations (e.g., big boulders, structures in the rock face, which are more stable than others) in both the 2014 TLS and the 2014 terrestrial photographs. A total of 39 GCPs were selected to ensure sufficient reference points in all terrestrial and webcam photographs, considering the geomorphologic changes between 2009 and 2016, and thus the appearance or disappearance of concise objects, especially in the earlier picture pairs (2009–2013). The 2014 terrestrial photographs serve, then, for localization of GCPs in the photographs from other time steps.
- Based on the sparse point cloud and using the available GCPs, the dense cloud of the 2014 terrestrial photographs was derived.
- After referencing the 2014 terrestrial photographs, the dense point cloud was exported as an LAS file and imported into RiSCAN Pro for an ICP adjustment. This was carried out between the 2014 LiDAR point cloud and the 2014 SfM point cloud, with the 2014 LiDAR point cloud serving as the “Master”.
- The final referenced 2014 SfM point cloud and the corresponding orthophotographs were used to identify and extract GCPs for referencing the webcam photographs. After

the final adjustment of the sparse cloud in AMP, a dense point cloud for each image pair of the webcam photographs was derived and exported as an LAS file.

- These LAS files were imported into RiSCAN Pro and an ICP adjustment was performed on the base of stable areas (Figure 4). This adjustment was necessary because uplift and subsidence had occurred in the area of the crater over the years due to active volcanism, making coordinates alone unreliable for fitting the individual point clouds. By using stable areas within the Areas of Interest (AoIs), these inconsistencies were avoided, assuming that these uplifts and subsidence did not occur at specific points but had approximately constant values in these areas.

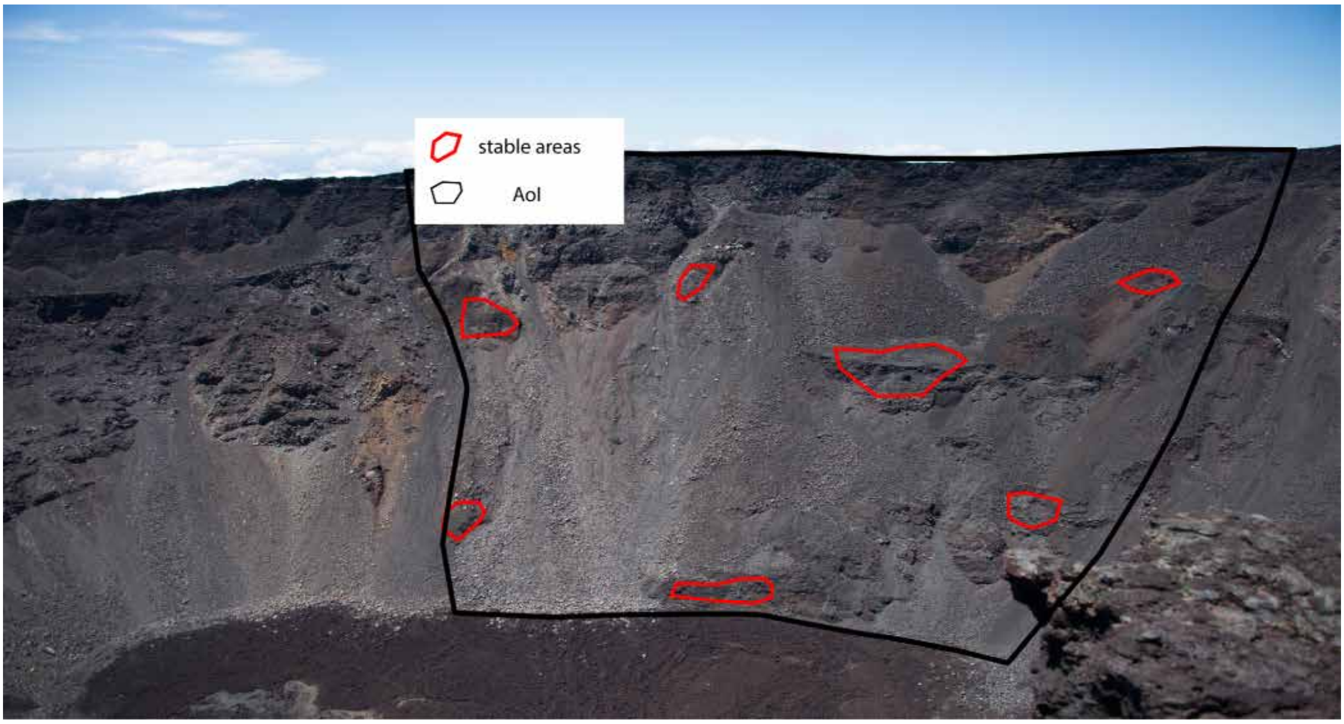

Figure 4. Investigated slope and stable areas for ICP adjustment. The location of the AoI can be seen in Figure 1 on the overview map of the crater.

At the end of this workflow, adjusted point clouds and orthophotographs are available for the different time steps. The point clouds were created as LAS files. The additional orthoimages were exported as referenced tiff files. All further processing steps (e.g., thinning, filtering, DEM generation) were performed similarly to the TLS and LiDAR data by using SAGA LIS.

3.5. Two-Step SfM and LiDAR Point Cloud Referencing

Given the significant differences in resolution, accuracy, and coverage among the various photogrammetric point clouds due to varying data quality [52,53], the goal was to reduce these discrepancies using the ICP algorithm (see Section 3.1). It was ensured that the co-registration was performed on data with similar point densities. To achieve this, the TLS point density was adjusted (“point cloud thinning”) to match the density of the corresponding SfM point clouds. Even after the first co-registration, the DTMs may still have some minor systematic errors. These were reduced by focusing on the stable surfaces in the vicinity of the respective process areas in a second co-registration step. Finally, all point clouds were exported as individual LAS files for further analysis.

3.6. Quantification of Surface Changes

The LAS files for all time steps, including TLS and SfM data, were imported to SAGA LIS Desktop (Vers. 3.0.7-64bit)/SAGA GIS (Vers. 3.1.0-64bit) by producing a SAGA point cloud. To eliminate flying points or artefacts, the "isolated point filter" and the "flying point filter" were applied (c.f. [45]). Deriving surface changes or the corresponding volumes by using a normal GIS system is challenging due to the poor representation of vertical areas. However, GIS systems provide many additional tools for spatial data analysis. LIS Desktop provides both 3D as well as 2.5D data formats and tools. Consequently, all surface changes and the corresponding volumes were derived in LIS by using the 3D point cloud data format. This was achieved by using the tool "distance between point clouds", which derives the 3D differences between corresponding points. These are defined using the point normal information. This normal information is in turn provided by a robust plane fitting approach, which is described in detail by [54]. Based on the 3D distances between corresponding points, areas with changes were mapped and DEMs of these areas for the single time steps were derived. Using these DEMs, the volume of each area was calculated by using the SAGA tool Cut & Fill [55] and by considering a Level of Detection (LoD).

3.7. Error Propagation

Since all point clouds contain inaccuracies due to measurement errors and registration inaccuracies, a LoD must be defined to differentiate measurement errors from actual topographic changes [54,56–58]. For calculating an LoD for the surface change calculation (point to point distances) of every single time step, a statistical approach of [57] using stable areas [59,60] was applied. The workflow, which is described in detail by [45] and [21] for the Cratère Dolomieu, uses the derived combined normal distribution error from the formula,

$$\delta_{point\ distance} = \sqrt{\sigma^2_{point\ distance} + \sigma^2_{point\ distance}}$$

where σ is the standard deviation of the derived point to point distances of assumed stable areas between two-time steps.

Following [60], the absolute value of each point to point distance (DP1−DP2) was divided by $\delta_{point\ distance}$ in order to calculate a t score:

$$t = \frac{|D_{P1} - D_{P2}|}{\delta_{point\ distance}}$$

Using a simple t-test ($t$crit at the 95% confidence interval with $t > 1.96$), the point to point distances can then be classified as probably real surface changes or probably measurement errors, and thus, an LoD can be derived for every single time step (Table 4). Point to point distances below the certain LoD were not used for the volume calculation.

Table 4. LoD derived from stable areas with corresponding used data sets.

Period	Data Set	LoD on Stable Areas
2010–2011	Webcam–webcam	0.59 m
2011–2012	Webcam–webcam	0.60 m
2012–2014	Webcam–TLS	0.69 m
2014–2015	TLS–terrestrial photographs	0.26 m
2015–2016	TLS–terrestrial photographs	0.45 m
2010–2016	Webcam–TLS	0.80 m

4. Results and Discussion

4.1. Useable Photographs for 4D Analysis

A total of 875 photos from the webcams were available between fall 2009 and 2012 to record changes in the southern crater area. In total, 485 of the photos are from the eastern camera and 390 from the western camera (Table 3). The data were carefully sifted and, unfortunately, most of the photos had to be discarded for the 4D analysis. For certain time periods, image pairs were not available due to memory issues, power supply failure, or incorrect time synchronization. Numerous photos were taken under bad weather conditions, like it is shown in Figure 5. As a result, no tie points can be found on the crater slopes during data processing.

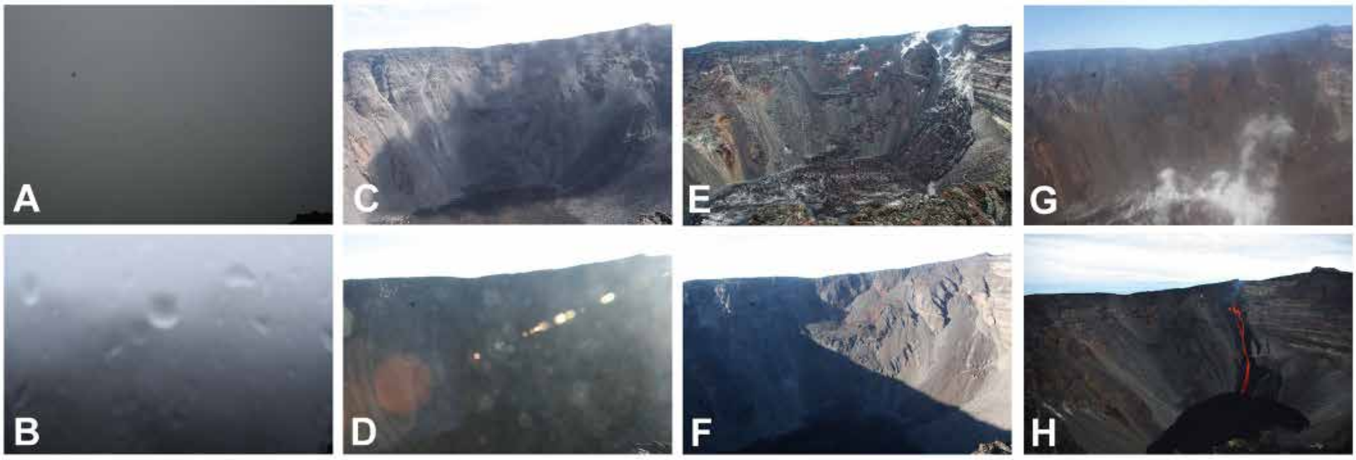

Figure 5. Different examples of photographs that were not usable for further SfM processing due to insufficiencies regarding differences in the quality. (**A**) Investigated slope was either completely or partially in clouds. (**B**) Camera lens was fogged. (**C**) Contamination on the camera lens. (**D**) Light reflections lead to a poor contrast. (**E**) Existing ground fog does not allow data processing. (**F**) Strong shadows especially during summer in the southern hemisphere led to contrast differences. (**G**) Existing fog in the crater. (**H**) Volcanic eruption occurred on 4 January 2010, moving lava prevented use of this image pair.

At the end of this review, 35 image pairs remained available for further 4D processing. For all these image pairs, a first alignment was calculated in AMP. After this first attempt, another 20 image pairs had to be discarded. In these image pairs, contrast and illumination differences, which at first glance were considered unproblematic, caused problems with the alignment. As a result, the software was unable to correctly reconstruct the respective lens distortion parameters and compute the appropriate camera model, which resulted in only a few tie points. This aligns with the findings of [61,62], who emphasize the critical role of image texture (entropy) in bundle adjustment and feature extraction (tie points) during SfM processing.

At the end of the process, it was decided to include photographs from January 2010, January 2011, and January 2012 for this study. With the TLS photos taken in November 2014, the photos taken in fall 2015, and the photos taken in fall 2016, this allowed similar periods to be processed in the analysis.

4.2. Achieved Accuracies

Based on the stable areas, an LoD could be calculated for the individual periods. The values of this LoD depend on the data used and it turns out that the point clouds calculated from webcam images in particular show higher values (Table 4). This applies, for example, to the periods 2010 to 2011 and 2011 to 2012, which were determined solely based on point clouds calculated from webcam images. The combination of webcam images and TLS data also shows a high LoD. In contrast, the combination of TLS data and the manually taken photographs provides the lowest values, with the period 2014 to 2015 showing the lowest LoD at 0.29 m, and 2015 to 2016 the second lowest with 0.45 m. Due to data gaps and the use of varying methods, different LoD values are to be expected. This indicates that the magnitudes observed differ across individual years. Small events cannot be detected in these data, which is, for example, not possible with the used webcam data sets. Due to the annual data, it is not clear whether the events were single or overlapping. However, the photographs provide some information that suggests that some of the events were single.

Nevertheless, it cannot be excluded that additional events occurred later. In this case, a higher temporal resolution of the data sets would be needed.

4.3. Mapping of Surface Changes Based on Webcam Photographs

To detect surface changes, the first step involved reviewing the photos of 2010 and 2016 to identify areas where major surface changes had occurred within the investigated period. These areas were then compared with the overlapping areas of the photographs to ensure that these active areas were within the derivable DTMs. At the end, four zones with visible major surface changes were identified. Although a large zone in the northern area with deposits is clearly visible in Figure 6, no surface changes could be quantified there. The areas were then mapped as polygons based on the SfM-derived orthophotos of the single time steps. These polygons were subsequently used as AoIs for the quantitative evaluations based on a DEM of differences (DoDs). Figure 6 shows these zones for 2010 and 2016. The perspectives of these photographs differ slightly because the photograph of 2010 was captured by the webcams, while the 2016 photograph was taken manually during a field survey. Consequently, the camera systems have different exposure angles. Nevertheless, surface changes between 2010 and 2016 are clearly visible. The most pronounced changes can be found at rockfall zone I.

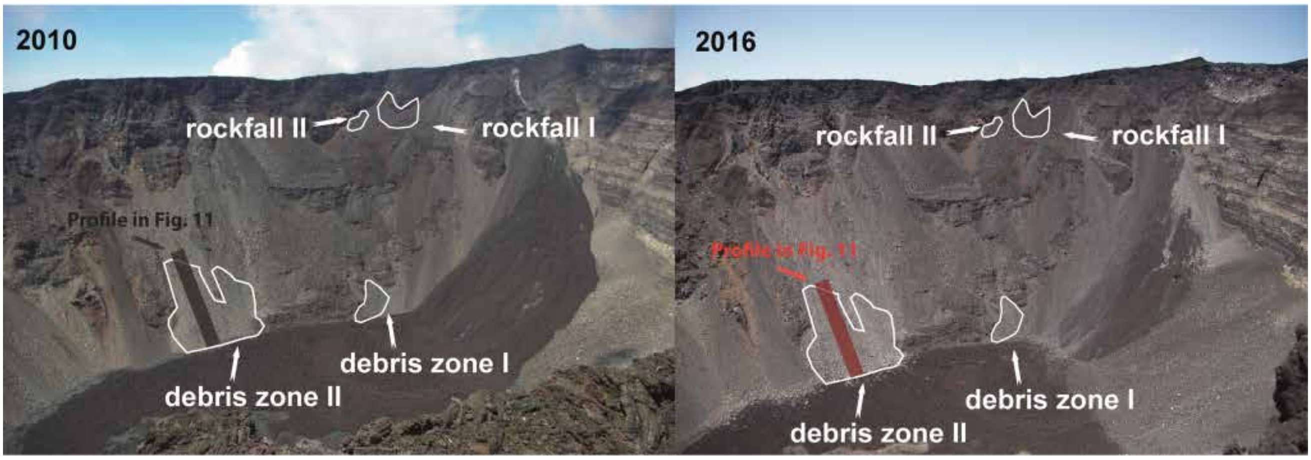

Figure 6. Mapped areas with visible surface changes within the different time steps between 2010 and 2016 that lie inside the derivable DTM. Both highlighted profile lines (grey, red) for the years 2010 and 2016 are analyzed in Figure 11.

4.4. Calculation of Surface Changes on the Mapped AoIs

4.4.1. Rockfall Zones

In the two rockfall zones (zones I and II), bigger deposits were observed below the bedrock areas (Figure 7). Due to the marginal position of the rock faces in the photographs and the limitations caused by the single overlap, surface changes in the rock faces could only be determined for the lower areas. For the adjacent scree slopes, however, we were able to quantify the deposits.

Throughout the study period, it is clearly visible that rockfall activity in rockfall zone I increased from 2010 to 2014 and decreased between 2014 and 2016. The accumulated material between 2010 and 2012 amounted to 1748 m^3 with a mean thickness of 20 cm between 2010 and 2011 and 11 cm between 2011 and 2012. From 2012 to 2014, the activity was an order of magnitude higher than during the previous period, totaling 16,799 m^3 with a mean thickness of nearly 3 m. This represents an annual deposition of almost 8400 m^3 and a mean annual thickness of almost 1.5 m.

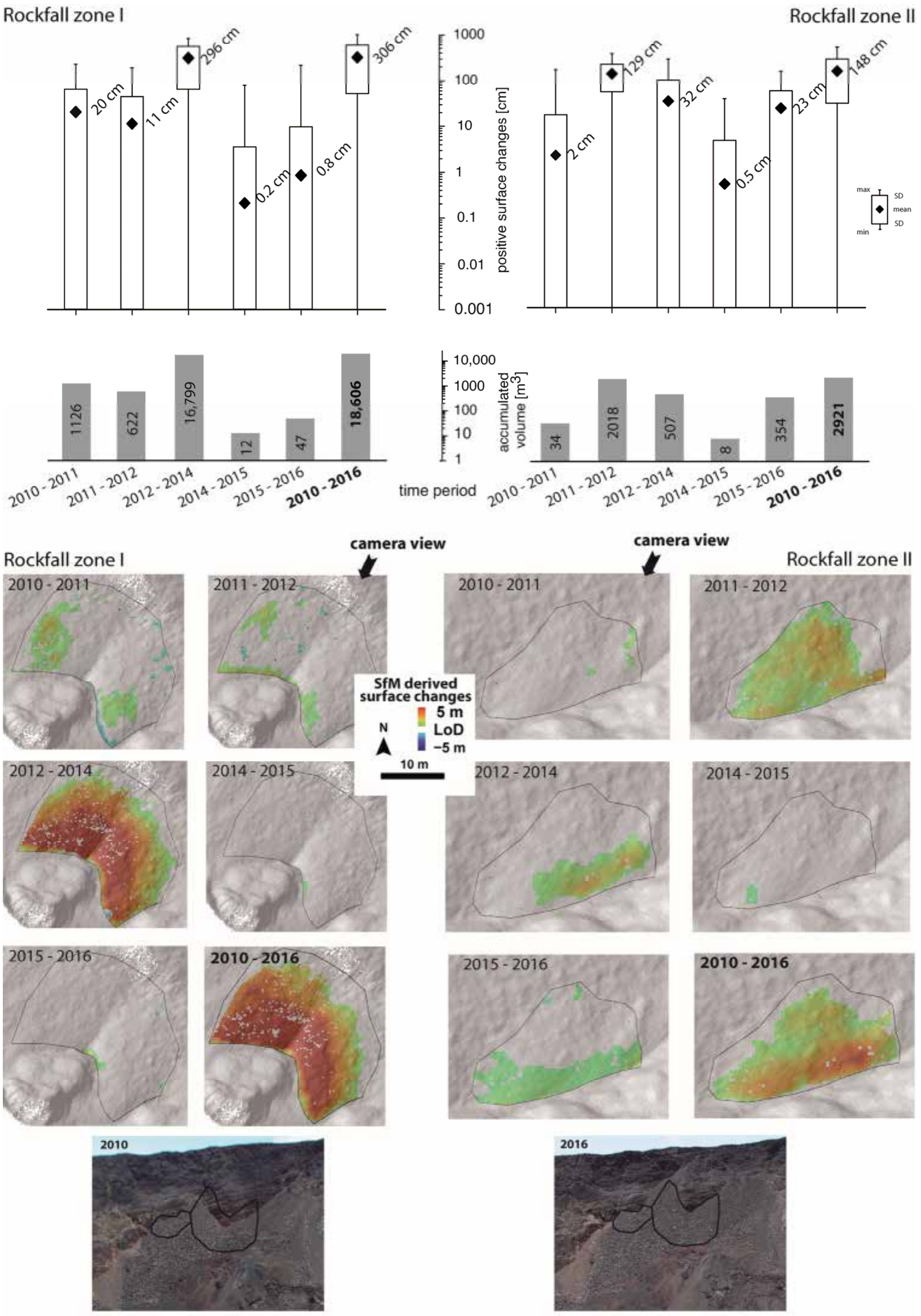

Figure 7. Derived surface changes (digital terrain model of differences: DoDs) for the two rockfall hotspots 1 and 2 between 2010 and 2016 (shaded relief in the background is derived on the base of the 2016 DTM). Also shown are the positive surface changes [cm] and the accumulated volume [m^3] of the two areas for the corresponding periods.

In addition to the quantification of the surface changes, the difference models reveal that accumulation on this scree slope is spatially very limited between 2010 and 2011, and between 2011 and 2012, likely due to smaller single events. This is also the conclusion reached by [21]. In their studies, they describe a decrease in activity in the years 2010 to 2011, which can be considered as a stable phase [21]. Between 2012 and 2014, a large-scale accumulation on the slope occurred, which can possibly be the consequence of a larger individual event. Even though no seismic activity could be detected for this period, one possible explanation for the destabilization is the combination of rainfall and strong winds caused by two tropical cyclones in early 2013 [22]. From 2014 onwards, only small surface changes are visible directly at the foot of the rock face, so that this area of the crater has apparently come to a temporal rest. While the activity of rockfalls is decreasing in this area of the crater, an increase can be observed in the northwestern area, also due to higher volcanic activity [21,22].

In rockfall zone II, no surface changes are visible between 2010 and 2011. Starting from 2011, an active phase begins, marked by a first large-scale accumulation with a volume of 2018 m^3 between 2011 and 2012, followed by a slightly lower accumulation of 507 m^3 between 2012 and 2014. After one year (2014 to 2015) with almost no activity, accumulation volumes of 354 m^3 were recorded between 2015 and 2016. The average surface changes between 2012 and 2014 and 2015 and 2016 were 32 cm and 23 cm, respectively. From 2011 until 2012, a mean accumulation height of 129 cm was detectable. The difference models of rockfall zone II clearly show that the accumulation is spatially very limited to areas close to the rock face between 2012 and 2014, and between 2015 and 2016, likely due to smaller single events with accumulation zones close to the rock face. The large-scale accumulation between 2011 and 2012 is probably the consequence of a larger individual event, which led to almost the entire rockfall zone II becoming an accumulation area.

For an area northwest of the Cratère Dolomieu, the authors of [21] were able to detect rockfalls with a volume of 80,000 m^3 during the study period from November 2014 to January 2016 in their survey based on TLS and terrestrial photogrammetry, among other methods. Increasing eruptive activity was detected in this period [22]. However, this area is not covered by the webcams, although if more permanent camera systems were to be installed on the crater rim, using photogrammetric principles, the entire slope and its processes could be captured. In a study on Volcán de Colima (Mexico) by [63], rockfall volumes were derived from high-resolution photographs. However, a conventional change detection study was not conducted. Instead, they categorized the rockfalls into several classes and calculated mean volumes for each. Their results showed mean volumes of 56.6 m^3, 43 m^3, and 146.7 m^3 [63], which are significantly lower than the values we calculated. In contrast, [1] measured significantly larger surface changes than ours over a comparable period (2011–2017) in their study of the Telica volcano in Nicaragua using an unmanned aerial vehicle (UAV). They recorded surface changes of 8400–140,000 m^3. It should be mentioned here that no process areas were detected, as we did. However, they do not provide a contextual classification of what triggered the observed surface changes, either.

4.4.2. Debris Zones

Within the investigated debris zones, surface changes are observable from 2010 to 2016 (Figure 8), with some exceeding one meter in height. Both zones are again located in the marginal area of the photos and at the transition between the debris cone and the crater floor. The photographs clearly indicate that the debris cones have expanded considerably to the crater floor, suggesting substantial accumulation in these areas.

In debris zone I, the activity was notably high between 2010 and 2014. During this period, 1821 m^3 of material accumulated between 2010 and 2011, followed by a slight accumulation of 107 m^3 between 2011 and 2012, and a higher accumulation of 1039 m^3 between 2012 and 2014. In total, 2967 m^3 of material was deposited during this period. The results up to 2012 are in good agreement with the investigations of [22], as the large surface changes in this phase of high seismic activity can be explained either by this or by rain. Even though a period of eruptive activity can be observed again from 2014 onwards [22], there was almost no accumulation in this area between 2014 and 2016. The average surface changes range between 10 cm and 110 cm between 2010 and 2014. After 2014, surface changes were minimal, and the deposition patterns do not clearly indicate whether the accumulation was due to landslide processes or fluvial deposits from sediment sources in their upper slope areas.

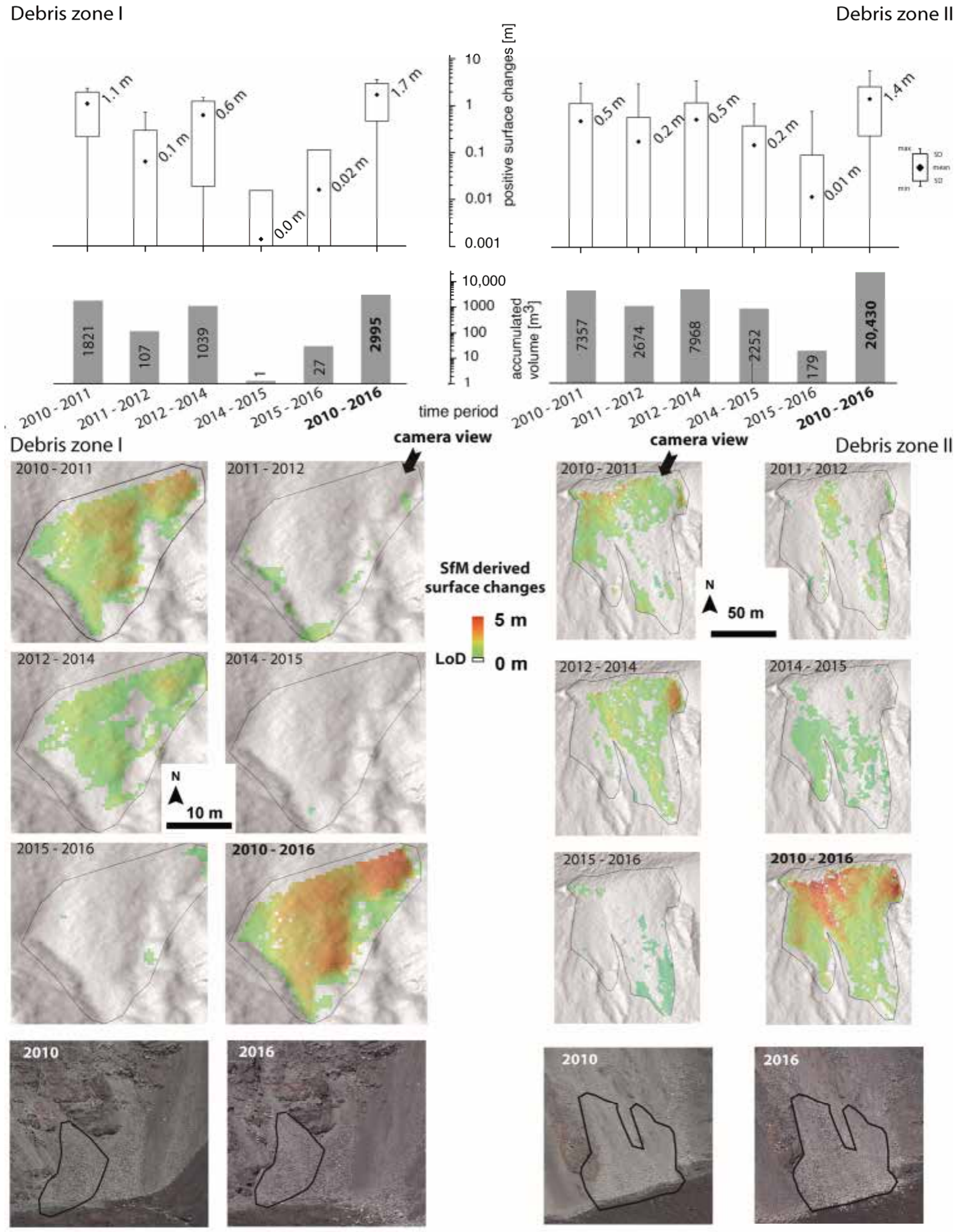

Figure 8. Derived surface changes (DoDs) on two selected debris cones between 2010 and 2016 (shaded relief in the background is derived on the base of the 2016 DTM). Also shown are the positive surface changes [cm] and the accumulated volume [m^3] of the two areas for the corresponding periods.

Debris zone II exhibits distinct linear depositional patterns, which indicate that the depositional area was formed by debris flows or fluvial processes. The high accumulation for the period 2012 to 2014 is presumably due to precipitation, since, as already mentioned, two cyclones occurred in 2013 [22]. However, larger individual boulders at the foot of the slope appear to have been deposited due to gravitational processes (falling stones) [64]. It is likely that different single processes formed the deposits. During fieldwork, gravitational processes (such as individual rockfall events or smaller rockfalls) were observed, and individual webcam images reveal linear structures that may indicate smaller debris flows (Figure 9).

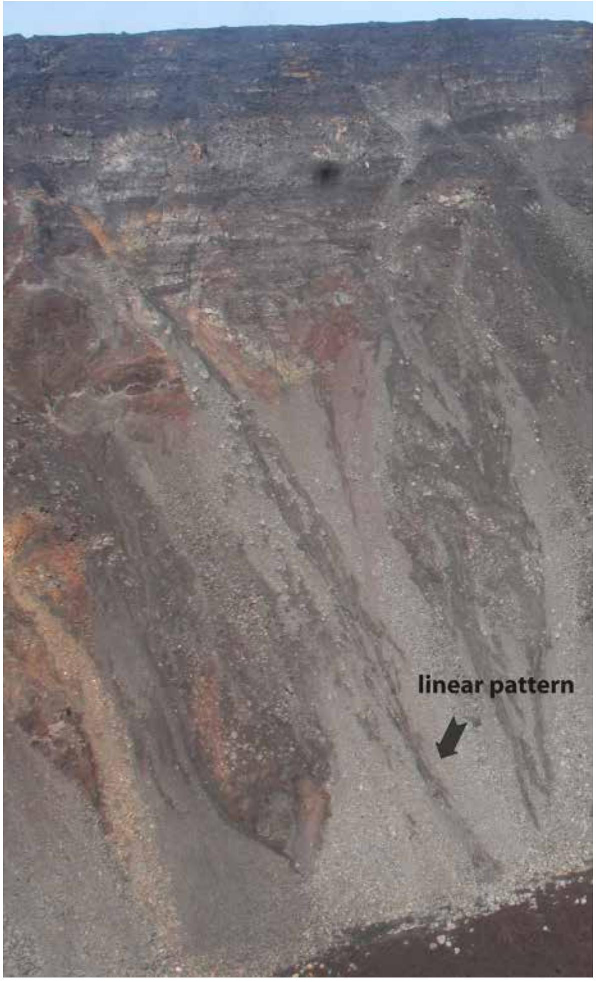

Figure 9. Clearly visible linear patterns on the debris zone II.

Overall, debris zone II is significantly larger than debris zone I and includes additional areas of loose material in the upper area, which transitions into rock areas in the uppermost area. According to the visual inspection, the upper areas have also changed over the observation period, but these zones lie outside the overlapping areas, so no DTMs could be calculated for them using SfM.

Due to increased eruptive activity, zone II like zone I shows increased accumulation in the first phase of the observation period [22]. The highest deposit volumes were recorded between 2010 and 2011 (7357 m^3), between 2011 and 2012 (2674 m^3), and between 2012 and 2014 (7968 m^3). In the period from 2012 to 2014, precipitation must be assumed to be the trigger [22]. After 2015, the activity decreases significantly to 179 m^3. The maximum value of the average surface change is 50 cm. Reference [15] calculated surface changes of $47.8 \pm 3.6 \times 10^3$ m^3 in another area of the Cratère Dolomieu using airborne SfM in their studies conducted from December 2014 to May 2015. It should be noted, however, that even if eruptive activity resumed during this period [22], this deposition occurred in the highly active northwestern area of the crater. Their analyses indicate that this large landslide occurred in mid-May 2015. For the whole period of their investigations from April 2008 to May 2015, they calculated a cumulative volume of $1.8 \pm 0.1 \times 10$ m^3 surface changes [15]. However, only processes larger than 1000 m^3 were quantified and the resolution of the data did not allow any conclusions to be drawn about possible triggering. Additionally, their investigations did not distinguish between different types of processes. The only event identified as a landslide was the one that occurred in April 2015. The investigations conducted by [65], who used TLS to collect data from various areas of a slope of the Vesuvius crater in 2005, 2006, and 2009, quantified surface changes amounting to a total volume of 20,300 m^3 across three areas. Their findings align closely with our results for debris zone II, which totaled 20,430 m^3. Another study, conducted with UAV-based photogrammetry on the slopes of Stromboli volcano, calculated surface changes of 21.5 m^3 for the period from December 2018 to June 2019 [17]. There is no differentiation by process type in their study either. Reference [66] shows volume changes of 210.08 m^3 in their studies at the active Lascar volcano in Chile with the use of a UAV for a period from 2017 to 2020. Appending the data, they were able to determine that a collapse occurred first, followed by rockfalls, and then the material was deposited as a landslide.

4.5. Temporal Specification of the Single Events

Since large events with strong surface changes should be visually recognizable in individual photographs, webcam photographs unsuitable for SfM processing were not used. With this approach of visual inspection of the photographs, a better temporal resolution of the process dynamics can be obtained. Existing studies have also successfully used single automatic cameras to detect single rockfall events (cf. [67]). All available webcam images were used and transformed into short films, zooming to the different zones to visualize surface changes (Figure 10). Only those photos with fog or wet lenses were excluded. Even if photographs are not suitable for SfM processing, the aim of this method was the identification of events and their confinement to a period between two photographs. For rockfall zone I, the major surface changes occurred after 2013, a period for which no webcam images were available. Consequently, the smaller surface changes between 2010 and 2012 could not be identified as single events.

Figure 10. The white arrows show visually detectable surface changes (DoDs) in rock zone II between 13 June 2011 and 19 June 2011.

In rockfall zone II, the highest surface changes occurred between 2011 and 2012. After reviewing the photographs, these changes were attributed to the period between 13 June 2011 and 19 June 2011 (Figure 10). Since no changes were visible before and after this period, it seems likely that the surface changes resulted from one major single event. Even though the photos provide evidence that individual processes occurred, it cannot be ruled out that other events took place at a later time. A higher temporal resolution of the data sets would be necessary in this case.

In the debris zones, most of the surface changes are within the period for which webcam images were available. For debris zone I, it could be determined that the lower scree slope was apparently built up successively by smaller single events, partly by individual rocks that were presumably transported gravitationally and deposited at the foot of the slope. Besides this successive deposition, however, a larger event occurred between 3 March 2010 and 16 March 2010, where material was transported linearly (fluvially or as a smaller debris flow) and then deposited as small cones at the base of the slope. Following this event, additional material was deposited, but no larger events were identified in the subsequent webcam photographs.

Continuous monitoring using webcam images is more difficult for the smaller debris zone II. However, the quantification results indicate a major surface change occurred between January 2010 and January 2011, as observed by [22] in their studies. Visual inspection of the webcam images indicated this change happened between 13 July 2010 and 2 December 2010. Unfortunately, no webcam images exist for the period between July and December 2010, preventing a more precise determination of the exact timing.

4.6. Geomorphic Perspective

The surface changes determined for the investigated slope show the high level of activity generally present within the crater, a finding consistent with other studies [15,21,22]. This high activity is largely attributable to the combination of high tectonic/seismic stress and the very high rainfall amounts on La Réunion. Reference [22] showed that rockfall activity, occurring about 2.5 years after the crater collapse, can be triggered by volcano tectonic seismicity and, to a lesser extent, rainfall. The sensitivity to seismic activity depends on the stability state of the crater walls. The observations of [21] show that even low seismicity ($M < 3$) at PLF can lead to increased rockfall activity. During the first 2.5 years post-collapse, the walls are so unstable that they fall without the need for external forcing. In the period without eruptive activity (2012–2014) and consequently with low seismic activity, it can be assumed that the main trigger is rain [22]. However, the high activity recorded in some areas between 2010 and 2016 is likely also due to the recent formation of the crater, indicating that the system remains in an unstable state. Following the crater collapse in 2007, steep slopes with unconsolidated material formed and were subsequently shaped by gravitational processes. While PLF is characterized by different eruptive phases during the observation period, the situation is different for the Telica volcano. It is constantly active and it can be assumed that the processes taking place are due to eruptive activity [1]. Unlike other mountainous areas, the debris cones are extremely young and the first webcam images from early 2010 capture the state of development after three years of geomorphological formation. Using the webcam images, the period of geomorphological development of the scree slopes can be extended from two years (2014 to 2016) to six years (2010 to 2016).

Figure 11A illustrates the slope development as a profile line (swath profile with a width of 25 m) from 2010 to 2016 (with only two profile lines shown here for better visibility). This indicates a slight flattening of the slope gradient over these six years. Figure 11B demonstrates that this flattening occurred successively and averaged around 1° slope inclination over these years. The statistical scattering range of the slope inclination has also decreased, an indicator that the slope is gradually stabilizing to a certain slope inclination and thus possibly to the slope angle of the prevailing substrate. The 35° slope inclination is in the upper range of the slope angles to be expected for scree slopes and is within the expected range as studies by [68–70] show. Reference [3] determined an average slope inclination of 33°. It is assumed that other process dynamics are responsible for this. In fact, lab experiments on granular layers submitted to high-frequency low-amplitude acoustic waves show that such waves may reduce by a few degree the avalanche angle (the maximum stability angle) of the granular layer by weakening intergranular friction [71]. Small-amplitude, high-frequency volcano tectonic seismicity may have a similar effect on the granular deposits on the slopes (see discussion in [22]). This could also be an indication that the investigated scree slope could be further flattened in the future and that the geomorphological development in this area was not yet complete in 2016.

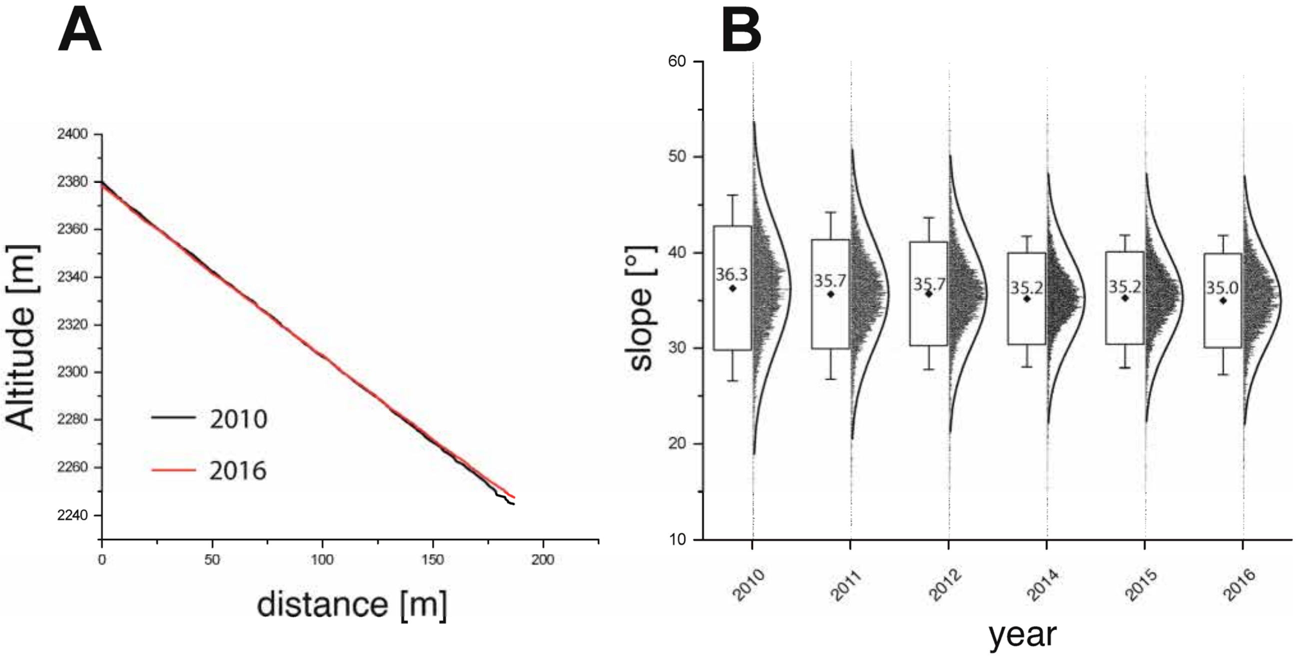

Figure 11. (**A**) The two lines are showing the slope development as a swath profile of debris zone II between 2010 and 2016. The location of the profile lines can be found in Figure 6. (**B**) Statistical range of the slope inclination for the years 2010 until 2016 showing a flattening of approximately 1°.

5. Conclusions

5.1. Methodological Aspect

From a methodological perspective, it can be asserted that using webcams for 4D analyses is only suitable in exceptional cases, when they are specifically installed for photogrammetric purposes at the time of installation. Despite the proximity of the webcams used in this study, the data processing was extremely complex. It required integrating LiDAR data in conjunction with photogrammetrically generated point clouds created from photos taken in parallel to the LiDAR mission. This integration allowed for the extraction of GCPs and fine referencing via ICP before converting the webcam images into 3D models and refining for quantitative investigations. Since the webcams were not initially intended for photogrammetric analysis, this meant that the camera positions were not ideal. Additionally, studies, particularly from the use of drone images for the creation of photogrammetric point clouds, show that overlap is crucial for minimizing errors in point cloud creation (c.f. [13]). In addition to the overlap values, the criteria specified for this include recommendations regarding the overlap directions (front- and sidelap). Due to using only two cameras, this study was limited to the sidelap, which limited the evaluable area of the slope to the central overlapping areas, and therefore, only slope sections (debris areas) that did not have complex 3D structures could be analyzed. Consequently, rock faces within the crater have a complex 3D surface and are additionally located at the marginal areas of the photographs, so those zones could not be analyzed. It therefore makes sense for future studies to extend the spatial resolution of the investigations for a process area by installing several webcams.

Nevertheless, the results indicate that webcam images can provide valuable information on geomorphological process dynamics by extending observation periods into the past and compressing them over time. Although not all photo pairs could be used for the 3D analysis in this case study, it was still possible to quantitatively assess individual periods. In addition, visual identification of process dynamics based on individual images allowed for some evaluation of the temporal development of the surface changes.

In the future, incorporating monoplotting tools alongside 3D evaluation could enhance the ability to make quantitative statements about process sequences, complementing visual inspection. In particular, since webcam recordings are rarely available as image pairs, focusing on monoplotting tools for retrospective analysis is advisable. Future studies should also consider integrating webcams/automatic cameras into monitoring studies to enable quantitative investigations. However, it is crucial that photogrammetric principles, such as overlap rates or overlap directions, be considered [13,18,72]. If photogrammetric principles are followed, webcam-based photographs provide significant potential for data recording, particularly in highly active geomorphological areas. This approach enables the differentiation and quantification of individual processes. Drawing from drone studies, using additional cameras with effective distribution (front- and sidelap) should significantly reduce processing effort and improve evaluation results.

5.2. Geomorphological Aspects

The slope section considered in this study represents a very young geomorphological form that has developed over a few years through a combination of gravitational mass movements (such as landslide processes and debris flows) and fluvial processes. This allows tracing the development of these slopes, which in the Alps typically takes centuries or even millennia after the glaciers melted, over an exceptionally short period. Although the first available data are only available from 2010, just three years after the original formation of the crater collapse, historical webcam images combined with LiDAR and terrestrial manual images enable the reconstruction of slope development over nearly six years.

The results indicate that the slope development begins with an initial formation phase that occurs rapidly within the first few years. Following this, the slope undergoes a more gradual progression from 2010 to 2016. This development leads to the slope eventually reaching an angle determined by the substrate. Even though it is not possible to distinguish between individual geomorphological processes, there is a demonstration of clear progression from the initial rapid formation to a more stable slope configuration over time. This adjustment of the slope inclination from 36.3° on average in 2010 to 35° on average in 2016 is still very rapid and clearly visible, possibly due to the decrease in the maximum stability angle of the granular material due to the cumulative effect of low-amplitude and high-frequency local seismicity [22,71]. As [3] describes the average slope angles as being 33°, it can be assumed that this adjustment process was not yet complete in 2016. Thus, a new survey of this slope area should be carried out in the future to check the extent to which the slope inclinations have developed since 2016.

The rate of adaption in this area is certainly influenced by the unique conditions at PLF. This region is volcanically very active, which causes surface movements, e.g., due to magma in the subsurface and seismic influences. Additionally, the volcanic material in the area of the rock faces has a very clear stratification, which was built up from basaltic lava and pyroclastics. These layers have varying degrees of stability, and combined with tectonic/seismic stress, this certainly enhances rock fall activity [73]. In some cases, the crater rim also features extensive deep crack formations, which further increases the instability of the rock faces. For example, Ref. [15] shows a rockfall with large magnitudes in the area of the eastern exposure of the crater, starting from such a crack. From a geomorphological perspective, the crater is ideally well-suited for current geomorphological process research, as these processes here occur at both very high frequency and, in some cases, with very high magnitudes. The spatially contained area (with a crater diameter of about 1 km) and the ideal observation perspective from the crater rim make it well-suited for observing with LiDAR or terrestrial photogrammetry. Therefore, it would also be beneficial to install similar fixed camera systems in other accessible craters. The only obstacle is the inability to enter the crater, which hampers the installation of stable survey points. Despite this, the area presents a promising opportunity for future research into geomorphological process dynamics using ground-based remote sensing techniques.

Author Contributions: Conceptualization, K.W. and F.H.; data curation, K.W. and F.H.; formal analysis, K.W. and F.H.; funding acquisition, A.M.; investigation, K.W., V.D., N.V., A.M., P.K., A.P., M.S. and F.H.; methodology, K.W. and F.H.; project administration, A.M., M.B. and F.H.; resources, N.V., A.M., P.K. and A.P.; software, K.W. and F.H.; supervision, F.H., A.M., M.S. and M.B.; validation, K.W., V.D., M.S. and F.H.; visualization, K.W.; writing—original draft preparation, K.W. and F.H.; writing—review and editing, K.W., V.D., N.V., A.M., A.P., M.S., M.B. and F.H. All authors have read and agreed to the published version of the manuscript.

Funding: This research received no external funding. The field trip for data acquisition on La Réunion and some discussions on the results were financed by ERC Contract No. ERC-CG-2013-PE10-617472 SLIDEQUAKES.

Data Availability Statement: The webcam-based data from the installed camera system and the climate station data was provided by the Volcanological Observatory of Piton de la Fournaise (Observatoire Volcanologique du Piton de la Fournaise, Institut de Physique du Globe de Paris (OVPF-IPGP, doi:10.18715/REUNION.OVPF). We thank the Service National d'Observation en Volcanologie (SNOV-CNRS-INSU) for the use of the database. The raw data supporting the conclusions of this article will be made available by the authors on request.

Acknowledgments: We would like to thank our colleagues at the Piton de la Fournaise Volcanological Observatory for their great support during the field work and data acquisition. In addition, we want to thank the four anonymous reviewers for their help to improve our manuscript.

Conflicts of Interest: The authors declare no conflicts of interest.

References

1. Hanagan, C.; La Femina, P.C.; Rodgers, M. Changes in Crater Morphology Associated With Volcanic Activity at Telica Volcano, Nicaragua. *Geochem. Geophys. Geosyst.* **2020**, *21*, e2019GC008889. [CrossRef]
2. Civico, R.; Ricci, T.; Scarlato, P.; Andronico, D.; Cantarero, M.; Carr, B.B.; De Beni, E.; Del Bello, E.; Johnson, J.B.; Kueppers, U.; et al. Unoccupied Aircraft Systems (UASs) Reveal the Morphological Changes at Stromboli Volcano (Italy) before, between, and after the 3 July and 28 August 2019 Paroxysmal Eruptions. *Remote Sens.* **2021**, *13*, 2870. [CrossRef]
3. Tournigand, P.-Y.; Smets, B.; Laxton, K.; Dille, A.; France, L.; Chazot, G.; Ho, C.; Wauthier, C.; Nicholson, E.J.; Kasanzu, H.C.; et al. Remote volcano monitoring using crowd-sourced imagery and Structure-from-Motion photogrammetry: A case study of Oldoinyo Lengai's active pit crater since the 2007–08 paroxysm. *J. Volcanol. Geotherm. Res.* **2023**, *443*, 107918. [CrossRef]
4. Geshi, N.; Shimano, T.; Chiba, T.; Nakada, S. Caldera collapse during the 2000 eruption of Miyakejima Volcano, Japan. *Bull. Volcanol.* **2002**, *64*, 55–68. [CrossRef]
5. Michon, L.; Staudacher, T.; Ferrazzini, V.; Bachèlery, P.; Marti, J. April 2007 collapse of Piton de la Fournaise: A new example of caldera formation. *Geophys. Res. Lett.* **2007**, *34*, 104. [CrossRef]
6. Duputel, Z.; Rivera, L. Show more The 2007 caldera collapse of Piton de la Fournaise volcano: Source process from very-long-period seismic signals. *Geoplanet-Earth Plan. Lett.* **2019**, *527*, 115786. [CrossRef]
7. Harnett, C.E.; Watson, R.A.; Holohan, E.P.; Schöpfer, M.P.J. Collapse caldera walls: Mechanical controls on slope failure and morphology. *J. Volcanol. Geotherm. Res.* **2023**, *442*, 107893. [CrossRef]
8. Klotz, S.; Le Bouteiller, C.; Mathys, N.; Fontaine, F.; Ravanat, X.; Olivier, J.-E.; Liébault, F.; Jantzi, H.; Coulmeau, P.; Richard, D.; et al. A high-frequency, long-term data set of hydrology and sediment yield: The alpine badland catchments of Draix-Bléone Observatory. *Earth Syst. Sci. Data* **2023**, *15*, 4371–4388. [CrossRef]
9. Barbarella, M.; Fiani, M.; Lugli, A. Landslide monitoring using multitemporal terrestrial laser scanning for ground displacement analysis. *Geomat. Nat. Hazards Risk* **2015**, *6*, 398–418. [CrossRef]
10. Pfeiffer, J.; Zieher, T.; Rutzinger, M.; Bremer, M.; Wichmann, V. Comparison and time series analysis of landslide displacement mapped by airborne, terrestrial and unmanned aerial vehicle based platforms. In Proceedings of the ISPRS Annals of the Photogrammetry, Remote Sensing and Spatial Information Sciences, ISPRS Geospatial Week, Enschede, The Netherlands, 10–14 June 2019.
11. Saito, H.; Uchiyama, S.; Hayakawa, Y.S.; Obanawa, H. Landslides triggered by an earthquake and heavy rainfalls at Aso volcano, Japan, detected by UAS and SfM-MVS photogrammetry. *Prog. Earth Planet Sci.* **2018**, *5*, 15. [CrossRef]
12. Carr, B.B.; Lev, E.; Vanderkluysen, L.; Moyer, D.; Marliyani, G.I.; Clarke, A.B. The Stability and Collapse of Lava Domes: Insight From Photogrammetry and Slope Stability Models Applied to Sinabung Volcano (Indonesia). *Front. Earth Sci.* **2022**, *10*, 813813. [CrossRef]
13. Stark, M.; Rom, J.; Haas, F.; Piermattei, L.; Fleischer, F.; Altmann, M.; Becht, M. Long-term assessment of terrain changes and calculation of erosion rates in an alpine catchment based on SfM-MVS processing of historical aerial images. How camera information and processing strategy affect quantitative analysis. *J. Geomorphol.* **2022**, *1*, 43–77. [CrossRef]
14. Ravanel, L.; Deline, P. Climate influence on rock-falls in high-Alpine steep rockwalls: The north side of the Aiguilles de Chamonix (Mont Blanc massif) since the end of the 'Little Ice Age'. *Holocene* **2010**, *21*, 357–365. [CrossRef]

15. Derrien, A.; Villeneuve, N.; Peltier, A.; Michon, L. Multi-temporal airborne structure-from-motion on caldera rim: Hazard, visitor exposure and origins of instabilities at Piton de la Fournaise. *Prog. Phys. Geogr. Earth Environ.* **2018**, *43*, 193–214. [CrossRef]
16. Guerin, A.; Stock, G.M.; Radue, M.J.; Jaboyedoff, M.; Collins, B.D.; Matasci, B.; Avdievitch, N.; Derron, M.-H. Quantifying 40 years of rockfall activity in Yosemite Valley with historical Structure-from-Motion photogrammetry and terrestrial laser scanning. *Geomorphology* **2020**, *356*, 107069. [CrossRef]
17. Gracchi, T.; Stefanelli, C.T.; Rossi, G.; Di Traglia, F.; Nolesini, T.; Tanteri, L.; Casagli, N. UAV-Based Multitemporal Remote Sensing Surveys of Volcano Unstable Flanks: A Case Study from Stromboli. *Remote Sens.* **2022**, *14*, 2489. [CrossRef]
18. Wegner, K.; Stark, M.; Haas, F.; Becht, M. Suitability of terrestrial archival imagery for SfM-MVS based surface reconstruction of steep rock walls for the detection of rockfalls. *J. Geomorphol.* **2023**. [CrossRef]
19. Rom, J.; Haas, F.; Hofmeister, F.; Fleischer, F.; Altmann, M.; Pfeiffer, M.; Heckmann, T.; Becht, M. Analysing the Large-Scale Debris Flow Event in July 2022 in Horlachtal, Austria Using Remote Sensing and Measurement Data. *Geosciences* **2023**, *13*, 100. [CrossRef]
20. Fontaine, F.R.; Roult, G.; Michon, L.; Barruol, G.; Di Muro, A. The 2007 eruptions and caldera collapse of the Piton de la Fournaise volcano (La Réunion Island) from tilt analysis at a single very broadband seismic station. *Geophys. Res. Lett.* **2014**, *41*, 2803–2811. [CrossRef]
21. Durand, V.; Mangeney, A.; Haas, F.; Jia, X.; Peltier, A.; Hibert, C.; Ferrazzini, V.; Kowalski, P.; Lauret, F.; Brunet, C.; et al. On the link between external forcings and slope instabilities in the Piton de la Fournaise summit crater, Reunion Island. *J. Geophys. Rev. Earth Surf.* **2018**, *123*, 2422–2442. [CrossRef]
22. Durand, V.; Mangeney, A.; Bernard, P.; Jia, X.; Bonilla, F.; Satriano, C.; Saurel, J.-M.; Aissaoui, E.M.; Peltier, A.; Ferrazzini, V.; et al. Repetitive small seismicity coupled with rainfall can trigger large slope instabilities on metastable volcanic edifices. *Commun. Earth Environ.* **2023**, *4*, 383. [CrossRef]
23. Suriñach, E.; Vilajosana, I.; Khazaradze, G.; Biescas, B.; Furdada, G.; Vilaplana, J.M. Seismic detection and characterization of landslides and other mass movements. *Nat. Hazards Earth Syst. Sci.* **2005**, *5*, 791–798. [CrossRef]
24. Walter, M.; Schwaderer, U.; Joswig, M. Seismic monitoring of precursory fracture signals from a destructive rockfall in the Vorarlberg Alps, Austria. *Nat. Hazards Earth Syst. Sci.* **2012**, *12*, 3545–3555. [CrossRef]
25. Nobile, A.; Acocella, V.; Ruch, J.; Aoki, Y.; Borgstrom, S.; Siniscalchi, V.; Geshi, N. Steady subsidence of a repeatedly erupting caldera through InSAR observations: Aso, Japan. *Bull. Volcanol.* **2017**, *79*, 32. [CrossRef]
26. Richter, N.; Froger, J.-L. The role of Interferometric Synthetic Aperture Radar in Detecting, Mapping, Monitoring, and Modelling the Volcanic Activity of Piton de la Fournaise, La Réunion: A Review. *Remote Sens.* **2020**, *12*, 1019. [CrossRef]
27. Vanneschi, C.; Di Camillo, M.; Aiello, E.; Bonciani, F.; Salvini, R. SfM-MVS photogrammetry for rock-fall analysis and hazard assessment along the ancient Roman Via Flaminia road at the Furlo Gorge (Italy). *ISPRS Int. J. Geo-Inf.* **2019**, *8*, 325. [CrossRef]
28. Gallo, I.G.; Martínez-Corbella, M.; Sarro, R.; Iovine, G.; López-Vinielles, J.; Hérnandez, M.; Robustelli, G.; Mateos, R.M.; García-Davalillo, J.C. An integration of UAV-based photogramme-try and 3D modelling for rockfall hazard assessment: The Cárcavos case in 2018 (Spain). *Remote Sens.* **2021**, *13*, 3450. [CrossRef]
29. Roncella, R.; Forlani, G.; Fornari, M.; Diotri, F. Landslide monitoring by fixed-base terrestrial stereo-photogrammetry. In Proceedings of the ISPRS Annals of the Photogrammetry, Remote Sensing and Spatial Information Sciences, ISPRS Technical Commission V Symposium, Riva del Garda, Italy, 23–25 June 2014.
30. Eltner, A.; Kaiser, A.; Abellan, A.; Schindewolf, M. Time lapse structure-from-motion photogrammetry for continuous geomorphic monitoring. *Earth Surf. Proc. Landf.* **2017**, *42*, 2240–2253. [CrossRef]
31. Kromer, R.; Walton, G.; Gray, B.; Lato, M.; Group, R. Development and Optimization of an Automated Fixed-Location Time Lapse Photogrammetric Rock Slope Monitoring System. *Remote Sens.* **2019**, *11*, 1890. [CrossRef]
32. Blanch, X.; Guinau, M.; Eltner, A.; Abellan, A. Fixed photogrammetric systems for natural hazard monitoring with high spatio-temporal resolution. *Nat. Hazards Earth Syst. Sci.* **2023**, *23*, 3285–3303. [CrossRef]
33. Falsaperla, S.; Neri, M.; Pecora, E.; Spampinato, S. Multidisciplinary study of flank instability phenomena at Stromboli volcano, Italy. *Geophys. Res. Lett.* **2006**, *33*, 15. [CrossRef]
34. Calvari, S.; Intrieri, E.; Di Traglia, F.; Bonaccorso, A.; Casagli, N.; Cristaldi, A. Monitoring crater-wall collapse at active volcanoes: A study of the 12 January 2013 event at Stromboli. *Bull. Volcanol.* **2016**, *78*, 39. [CrossRef]
35. Coltelli, M.; d'Aranno, P.J.V.; de Bonis, R.; Tello, J.F.G.; Marsella, M.; Nardinocchi, C.; Pecora, E.; Proietti, C.; Scifoni, S.; Scutti, M.; et al. The Use of Surveillance Cameras for the Rapid Mapping of Lava Flows: An Application to Mount Etna Volcano. *Remote Sens.* **2017**, *9*, 192. [CrossRef]
36. Barnie, T.; Hjörvar, T.; Titos, M.; Sigurðsson, E.M.; Pálsson, S.K.; Bergsson, B.; Ingvarsson, Þ.; Pfeffer, M.A.; Barsotti, S.; Arason, Þ.; et al. Volcanic plume height monitoring using calibrated web cameras at the Icelandic Meteorological Office: System overview and first application during the 2021 Fagradalsfjall eruption. *J. Appl. Volcanol.* **2023**, *12*, 4. [CrossRef]
37. Michon, L.; Saint-Age, F. Morphology of Piton de la Fournaise basaltic shield volcano (La Réunion Island): Characterization and implication in the volcano evolution. *J. Geophys. Res.* **2008**, *113*, 2156–2202. [CrossRef]
38. Le Friant, A.; Lebas, E.; Clément, V.; Boudon, G.; Deplus, C.; De Voogd, B.; Bachèlery, P. A new model for the evolution of La Réunion volcanic complex from complete marine geophysical surveys. *Geophys. Res. Lett.* **2011**, *38*, 39. [CrossRef]
39. Gillot, P.-Y.; Lefèvre, J.-C.; Nativel, P.E. Model for the structural evolution of the volcanoes of Réunion island. *Earth Planet. Sci. Lett.* **1994**, *122*, 291–302. [CrossRef]

40. Famin, V.; Paquez, C.; Danišík, M.; Gardiner, N.J.; Michon, L.; Kirkland, C.L.; Berthod, C.; Friedrichs, B.; Schmitt, A.K.; Monié, P. Multitechnique geochronology of intrusive and explosive activity on Piton des Neiges Volcano, Réunion Island. *Geochem. Geophys. Geosyst.* **2022**, *23*, e2021GC010214. [CrossRef]
41. Lénat, J.-F.; Bachèlery, P. Dynamics of magma transfer at Piton de la Fournaise volcano (Réunion Island, Indian Ocean). In *Modeling of Volcanic Processes. Earth Evolution Sciences*; King, C.-Y., Scarpa, R., Eds.; Vieweg+Teubner Verlag: Wiesbaden, Germany, 1988; pp. 57–72.
42. Staudacher, T.; Ferrazzini, V.; Peltier, A.; Kowalski, P.; Boissier, P.; Catherine, P.; Lauret, F.; Massin, F. The April 2007 eruption and the Doloieu crater collapse, two major events at Piton de la Fournaise (La Réunion Island, Indian Ocean). *J. Volcanol. Geotherm. Res.* **2009**, *184*, 126–137. [CrossRef]
43. Garcin, M.; Poisson, B.; Pouget, R. High rates of geomorphological processes in a tropical area: The Remparts river case study (Réunion Island, Indian Ocean). *Geomorphology* **2005**, *67*, 335–350. [CrossRef]
44. Join, J.-L.; Folio, J.-L.; Bourhane, A.; Comte, J.-C. Groundwater Resources on Active Basaltic Volcanoes: Conceptual Models from La Réunion Island and Grande Comore. In *Active Volcanoes of the Southwest Indian Ocean Piton de la Fournaise and Karthala*; Bachèlery, P., Lénat, J.-F., Di Muro, A., Michon, L., Eds.; Springer: Berlin/Heidelberg, Germany, 2016; pp. 61–70.
45. Haas, F.; Hilger, L.; Neugirg, F.; Umstädter, K.; Breitung, C.; Fischer, P.; Hilger, P.; Heckmann, T.; Dusik, J.; Kaiser, A.; et al. Quantification and analysis of geomorphic processes on a recultivated iron ore mine on the Italian island Elba using long-time ground-based LIDAR and photogrammetric data by an UAV. *Nat. Hazards Earth Syst. Sci.* **2016**, *16*, 1269–1288. [CrossRef]
46. Zhang, Z. Iterative point matching for registration of free-form curves and surfaces. *Int. J. Comput. Vis.* **1994**, *13*, 119–152. [CrossRef]
47. Micheletti, N.; Chandler, J.H.; Lane, S.N. Investigating the geomorphological potential of freely available and accessible structure-from-motion photo-grammetry using a smartphone. *Earth Surf. Proc. Landf.* **2015**, *40*, 473–486. [CrossRef]
48. Riegl VZ-4000. Available online: http://www.riegl.com/uploads/tx_pxpriegldownloads/RIEGL_VZ-4000_Datasheet_2020-09-14.pdf (accessed on 10 September 2024).
49. Conrad, O.; Bechtel, B.; Bock, M.; Dietrich, H.; Fischer, E.; Gerlitz, L.; Wehber, J.; Wichmann, V.; Böhner, J. System for Automated Geoscientific Analyses (SAGA) v. 2.1.4. *Geosci. Model Dev.* **2015**, *8*, 1991–2007. [CrossRef]
50. Westoby, M.J.; Brasington, J.; Glasser, N.F.; Hambrey, M.J.; Reynolds, J.M. 'Structure-from-Motion' photogrammetry: A low-cost, effective tool for geoscience applications. *Geomorphology* **2012**, *179*, 300–314. [CrossRef]
51. James, M.R.; Robson, S.; d'Oleire-Oltmanns, S.; Niethammer, U. Optimising UAV topographic surveys with structure-from-motion: Ground control quality, quantity and bundle adjustment. *Geomorphology* **2017**, *280*, 51–66. [CrossRef]
52. James, M.R.; Robson, S.; Smith, M.W. 3-D uncertainty-based topographic change detection with structure-from-motion photogrammetry: Precision maps for ground control and directly georeferenced surveys. *Earth Surf. Proc. Landf.* **2017**, *42*, 1769–1788. [CrossRef]
53. James, M.R.; Antoniazza, G.; Robson, S.; Lane, S.N. Mitigating systematic error in topographic models for geomorphic change detection: Accuracy, precision and considerations beyond off-nadir imagery. *Earth Surf. Proc. Landf.* **2020**, *45*, 2251–2271. [CrossRef]
54. Fey, C.; Wichmann, V. Long-range terrestrial laser scanning forgeomorphological change detection in alpineterrain—Handling uncertainties. *Earth Surf. Proc. Landf.* **2017**, *42*, 789–802. [CrossRef]
55. Heckmann, T. Cut & Fill module for SAGA GIS 2.2.0. 2006.
56. Brasington, J.; Langham, J.; Rumsby, B. Methodological sensitivity of morphometric estimates of coarse fluvial sediment transport. *Geomorphology* **2003**, *53*, 299–316. [CrossRef]
57. Lane, S.N.; Westaway, R.M.; Murray, H.D. Estimation of erosion and deposition volumes in a large, gravel-bed, braided river using synoptic remote sensing. *Earth Surf. Proc. Landf.* **2003**, *28*, 249–271. [CrossRef]
58. Bennett, G.L.; Molnar, P.; Eisenbeiss, H.; McArdell, B.W. Erosiononal power in the Swiss Alps: Characterization of slope failure in the Illgraben. *Earth Surf. Proc. Landf.* **2012**, *37*, 1627–1640. [CrossRef]
59. Brasington, J.; Rumsby, B.T.; McVey, R.A. Monitoring and modelling morphological change in a braided gravel-bed river using high resolution GPS-based survey. *Earth Surf. Proc. Landf.* **2000**, *25*, 973–990. [CrossRef]
60. Westaway, R.M.; Lane, S.N.; Hicks, D.M. The development of an automated correction procedure for digital photogrammetry for the study of wide, shallow, gravel bed rivers. *Earth Surf. Proc. Landf.* **2000**, *25*, 209–226. [CrossRef]
61. Gomez, C.; Hayakawa, Y.; Obanawa, H. A study of Japanese landscapes using structure from motion derived DSMs and DEMs based on historical aerial photographs: New opportunities for vegetation monitoring and diachronic geomorphology. *Geomorphology* **2015**, *242*, 11–20. [CrossRef]
62. Bakker, M.; Lane, S.N. Archival photogrammetric analysis of river-floodplain systems using Structure from Motion (SfM) methods. *Earth Surf. Proc. Landf.* **2017**, *42*, 1274–1286. [CrossRef]
63. Mueller, S.B.; Varley, N.R.; Kueppers, U.; Lesage, P.; Reyes Davila, G.A.; Dingwell, D.B. Quantification of magma ascent rate through rockfall monitoring at the growing/collapsing lava dome of Volc'an de Colima, Mexico. *Solid Earth* **2013**, *4*, 201–213. [CrossRef]
64. Kuehnert, J.; Mangeney, A.; Capdeville, Y.; Vilotte, J.P.; Stutzmann, E.; Chaljub, E.; Aissaoui, M.; Boissier, P.; Brunet, C.; Kowalski, P.; et al. Rockfall localization based on inter-station ratios of seismic energy. *J. Geophys. Res.—Earth Surface* **2021**, *126*. [CrossRef]

65. Pesci, A.; Teza, G.; Casula, G.; Fabris, M.; Bonforte, A. Remote Sensing and Geodetic Measurements for Volcanic Slope Monitoring: Surface Variations Measured at Northern Flank of La Fossa Cone (Vulcano Island, Italy). *Remote Sens.* **2011**, *5*, 2238–2256. [CrossRef]
66. Ai, L.; Walter, T.R.; Aguilera, F.; Layana, S.; Mania, R.; Kujawa, C.; Zimmer, M.; Inostroza, M. Crater morphology, nested ring structures, and temperature anomalies studied by unoccupied aircraft system data at Lascar volcano, northern Chile. *J. Volcanol. Geotherm. Res.* **2023**, *439*, 107840. [CrossRef]
67. Mourey, J.; Lacroix, P.; Duvillard, P.A.; Marsy, G.; Marcer, M.; Malet, E.; Ravanel, L. Multi method monitoring of rockfall activityalong the classic route up Mont Blanc (4809 m a.s.l.) to encourage adaption by mountaineers. *Nat. Hazards Earth Syst. Sci.* **2022**, *22*, 445–460. [CrossRef]
68. Chandler, R.J. The Inclination of Talus, Arctic Talus Terraces, and Other Slopes Composed of Granular Materials. *J. Geol.* **1973**, *81*, 1–14. [CrossRef]
69. Carson, M.A. Angles of Repose, Angles of Shearing Resistance and Angles of Talus Slopes. *Earth Surface Process.* **1977**, *2*, 363–380. [CrossRef]
70. van Steijna, H.; Boelhouwers, J.; Harris, S.; Hétu, B. Recent research on the nature, origin and climatic relations of blocky and stratified slope deposits. *Prog. Phys. Geogr.* **2002**, *26*, 551–575. [CrossRef]
71. Léopoldès, J.; Jia, X.; Tourin, A.; Mangeney, A. Triggering granular avalanches with ultrasound. *Phys. Rev. E* **2020**, *102*, 042901. [CrossRef]
72. Eltner, A.; Kaiser, A.; Castillo, C.; Rock, G.; Neugirg, F.; Abellán, A. Image-based surface reconstruction in geomorphometry—Merits, limits and developments. *Earth Surf. Dyn.* **2016**, *4*, 359–389. [CrossRef]
73. Chen, Y.; Remy, D.; Froger, L.J.; Peltier, A.; Villeneuve, N.; Darrozes, J.; Perfettini, H.; Bonvalot, S. Long term ground displacement using InSAR and GNSS at Piton de la Fournaise volcano between 2009 and 2014. *Remote Sens. Environ.* **2017**, *194*, 230–247. [CrossRef]